CHEMISTRY OF MATERIALS
Cite This: Chem. Mater. XXXX, XXX, XXX−XXX
Article
pubs.acs.org/cm

Engineering Two-Phase and Three-Phase Microstructures from Water-Based Dispersions of Nanoparticles for Eco-Friendly Polymer Solar Cell Applications

Natalie P. Holmes,*[,†,‡,▲] Melissa Marks,[†,▲] James M. Cave,[⊥] Krishna Feron,[†] Matthew G. Barr,[†] Adam Fahy,[†] Anirudh Sharma,[¶,#] Xun Pan,[¶] David A. L. Kilcoyne,[∥] Xiaojing Zhou,[†] David A. Lewis,[¶] Mats R. Andersson,[¶] Jan van Stam,[§] Alison B. Walker,[⊥] Ellen Moons,[‡] Warwick J. Belcher,[†] and Paul C. Dastoor[†]

[†]Centre for Organic Electronics, University of Newcastle, University Drive, Callaghan New South Wales 2308, Australia
[‡]Department of Engineering and Physics and [§]Department of Engineering and Chemical Sciences, Karlstad University, 65188 Karlstad, Sweden
[⊥]Department of Physics, University of Bath, Bath BA2 7AY, United Kingdom
[¶]Flinders Institute for Nanoscale Science and Technology, Flinders University, Sturt Road, Bedford Park, Adelaide, South Australia 5042, Australia
[#]Laboratoire de Chimie des Polymères Organiques (LCPO), University of Bordeaux, UMR 5629, B8 Allée Geoffroy Saint Hilaire, 33615 Pessac Cedex, France
[∥]Advanced Light Source, Lawrence Berkeley National Laboratory, Berkeley, California 94720, United States

Supporting Information

ABSTRACT: Nanoparticle organic photovoltaics, a subfield of organic photovoltaics (OPV), has attracted increasing interest in recent years due to the eco-friendly fabrication of solar modules afforded by colloidal ink technology. Importantly, using this approach it is now possible to engineer the microstructure of the light absorbing/charge generating layer of organic photovoltaics; decoupling film morphology from film deposition. In this study, single-component nanoparticles of poly(3-hexylthiophene) (P3HT) and phenyl-C_{61} butyric acid methyl ester ($PC_{61}BM$) were synthesized and used to generate a two-phase microstructure with control over domain size prior to film deposition. Scanning transmission X-ray microscopy (STXM) and electron microscopy were used to characterize the thin film morphology. Uniquely, the measured microstructure was a direct input for a nanoscopic kinetic Monte Carlo (KMC) model allowing us to assess exciton transport properties that are experimentally inaccessible in these single-component particles. Photoluminescence, UV−vis spectroscopy measurements, and KMC results of the nanoparticle thin films enabled the calculation of an experimental exciton dissociation efficiency (η_{ED}) of 37% for the two-phase microstructure. The glass transition temperature (T_g) of the materials was characterized with dynamic mechanical thermal analysis (DMTA) and thermal annealing led to an increase in η_{ED} to 64% due to an increase in donor−acceptor interfaces in the thin film from both sintering of neighboring opposite-type particles in addition to the generation of a third mixed phase from diffusion of $PC_{61}BM$ into amorphous P3HT domains. As such, this study demonstrates the higher level of control over donor−acceptor film morphology enabled by customizing nanoparticulate colloidal inks, where the optimal three-phase film morphology for an OPV photoactive layer can be designed and engineered.

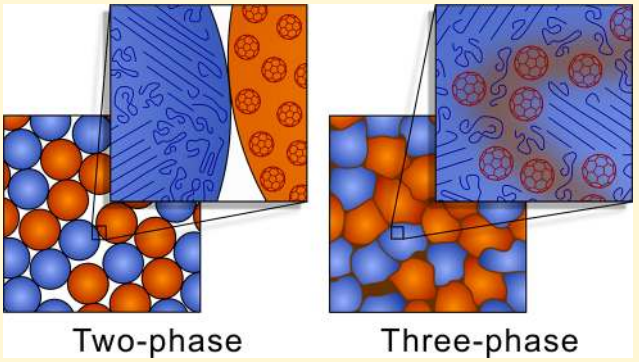

INTRODUCTION

Polymer solar cells (organic photovoltaics) are a competitive third generation solar cell technology due to their light-weight, flexibility, low-cost fabrication, and absence of heavy metals.[1] A bulk heterojunction (BHJ) photoactive layer is typically employed in polymer solar cells that is processed almost exclusively from toxic organic solvents (such as chlorobenzene, 1,2-dichlorobenzene, and chloroform).[2−4] Unfortunately, using these toxic organic solvents to print polymer solar cells on a mass scale is not feasible since it increases the cost of production, is

Received: July 30, 2018
Revised: August 16, 2018
Published: August 17, 2018

DOI: 10.1021/acs.chemmater.8b03222
Chem. Mater. XXXX, XXX, XXX−XXX

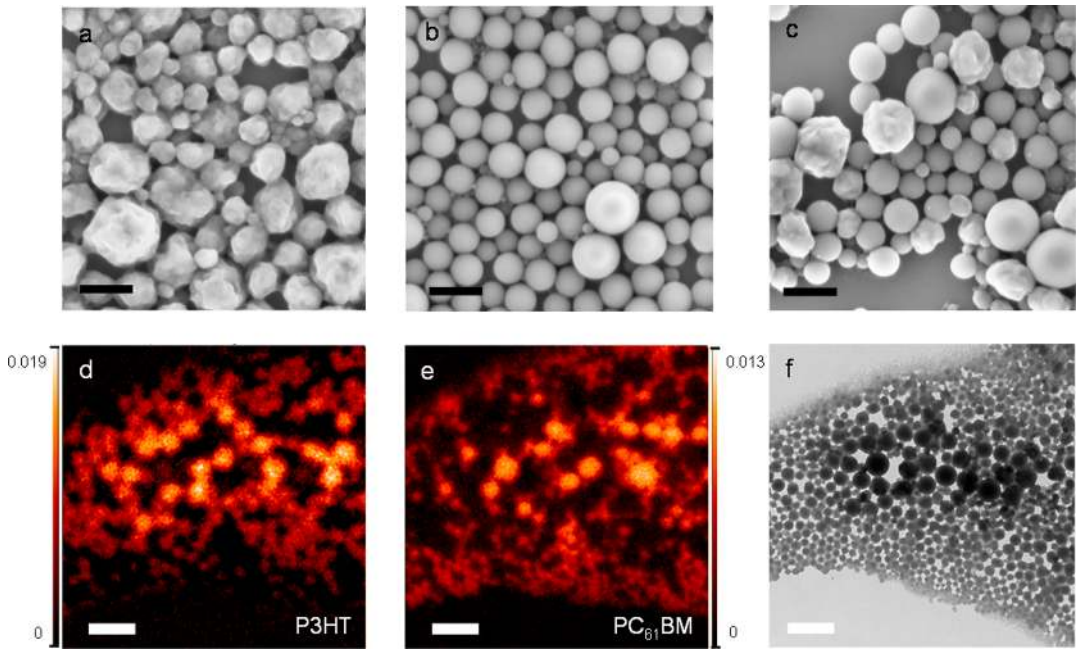

Figure 1. SEM image of (a) pristine P3HT nanoparticles, (b) pristine $PC_{61}BM$ nanoparticles, (c) P3HT nanoparticles mixed with $PC_{61}BM$ nanoparticles ($P3HT_{NP}$:$PC_{61}BM_{NP}$) (scales bars are 200 nm in a–c). STXM mass plots showing concentration of (d) P3HT and (e) $PC_{61}BM$ in a $P3HT_{NP}$:$PC_{61}BM_{NP}$ film (T0) (scale bars are 600 nm in panels d and e). The color scale bars indicate concentration of component in mg/cm^2. (f) Position-matched TEM for the $P3HT_{NP}$:$PC_{61}BM_{NP}$ film in panels d and e. Scale bar in f is 600 nm.

harmful to worker health, and is undesirable from an environmental perspective.[4] As such, developing eco-friendly processing technologies for solar cells is a recent target of the polymer solar cell community,[5] a key approach being the preparation of nanoparticulate colloidal inks, which enables the deposition of photoactive layers from water.[6−11]

Depositing polymer solar cell photoactive layers from nanoparticles also affords the unique opportunity to engineer the thin film morphology on the nanoscale. An optimal photoactive layer morphology is key to efficient OPV device performance,[12−15] with fine-scale phase separation of the polymer donor and fullerene acceptor required to achieve a high exciton dissociation efficiency and short-circuit current density (J_{SC}).[16,17] If the polymer and fullerene domain sizes are much larger than the exciton diffusion length in the semiconductor materials, exciton diffusion can become the limiting factor for charge generation.[18] Nanoparticle photoactive layers represent a new and interesting opportunity for tailoring the donor−acceptor domain size to the nanoscale.[19,20] The donor and acceptor material domain sizes can be preset prior to film deposition by controlling the nanoparticle size during fabrication, which can be achieved by modifying synthesis parameters such as surfactant concentration, as demonstrated in our previous work.[10] Intermixing of the donor and acceptor material can then be carefully controlled by applying thermal treatments to the films at temperatures close to the material glass transition temperature (T_g).

Our previous reports of nanoparticle organic photovoltaics have been based on colloidal nanoparticle inks synthesized via the mini-emulsion route and adding both polymer donor and fullerene acceptor materials to the mini-emulsion's dispersed phase, leading to core−shell binary nanoparticles.[8,10,21−25] This dominant core−shell nanoparticle morphology consists of a polymer-rich shell and a fullerene-rich core, with the purity of the core and shell phases depending on the synthesis parameters, which can often be difficult to control. By comparison, the optimal solvent-cast BHJ regioregular P3HT:$PC_{61}BM$ system is reported to be fundamentally a three-phase system if suitable annealing conditions are applied, with pure $PC_{61}BM$ and crystalline pure P3HT phases in addition to a mixed amorphous P3HT:$PC_{61}BM$ third phase.[26,27]

In contrast to the wealth of literature on both BHJ and core−shell nanoparticle systems, only few studies exist of combined pristine nanoparticle systems for OPV and, to date, limited work has been reported on the use of these systems to control film morphology.[9,28] In particular, there have been no reports on whether it is possible to generate a three-phase microstructured film from a precisely controlled two-phase film. In this paper, we directly engineer both two-phase and three-phase thin film morphologies from pristine donor polymer nanoparticles and pristine acceptor fullerene nanoparticles. By carefully combining and annealing these nanoparticles, a three-phase thin film morphology is generated in a more controlled environment than both BHJ and core−shell nanoparticle systems. This study highlights the advantages nanoparticles offer the field of organic photovoltaics by enabling film morphologies to be designed and engineered.

RESULTS AND DISCUSSION

Organic Nanoparticle Synthesis. Pristine P3HT nanoparticles ($P3HT_{NP}$) and pristine $PC_{61}BM$ nanoparticles ($PC_{61}BM_{NP}$) were synthesized using the mini-emulsion method as reported previously by our group.[10,23] The nanoparticle size was measured by applying a circular Hough transform algorithm to SEM images of nanoparticle films.[10] This method gave mean diameters of 150 ± 40 nm for the P3HT nanoparticles and 118 ± 41 nm for the $PC_{61}BM$ nanoparticles. These particle sizes have been tailored to optimize both STXM and SEM imaging. The SEM and particle size distribution plots are presented in Figure S1 for both particle types (Supporting Information). Impor-

DOI: 10.1021/acs.chemmater.8b03222
Chem. Mater. XXXX, XXX, XXX−XXX

tantly, the nanoparticle size can be easily reduced to more closely match the exciton diffusion length in organic semiconductors by adjusting the nanoparticle synthesis parameters,[10] for example, by either increasing the concentration of surfactant in the miniemulsion aqueous phase (as we have demonstrated with a series of nanoparticle inks in Figure S2) or alternatively by decreasing the concentration of semiconducting material in the miniemulsion oil phase.[20]

Thin Film Morphology: Two-Phase Microstructure. To generate a film with a two-phase microstructure, pristine P3HT nanoparticles were combined with pristine $PC_{61}BM$ nanoparticles and the resultant $P3HT_{NP}$:$PC_{61}BM_{NP}$ ink utilized to spin coat films. The packing of the $P3HT_{NP}$:$PC_{61}BM_{NP}$ film is mostly a randomly close packed (RCP) array (Figure 1c). The pristine P3HT nanoparticles also pack in a mostly RCP array (Figure 1a), whereas the pristine $PC_{61}BM$ nanoparticles form both RCP arrays and hexagonally close packed (HCP) arrays (Figure S3).

Detailed microscopy of the two-phase microstructured film enabled the nanoparticle types (and hence domain/phase type) to be identified via two means: (1) the chemical sensitivity of near edge X-ray absorption fine structure (NEXAFS) spectra at the C-edge, employed by scanning transmission X-ray microscopy (STXM), and (2) the shape and surface texture of P3HT nanoparticles versus $PC_{61}BM$ nanoparticles evident in SEM. STXM maps of the $P3HT_{NP}$:$PC_{61}BM_{NP}$ films are presented in Figure 1d and e. The P3HT map (Figure 1d), collected at an X-ray energy of 285.3 eV, and the $PC_{61}BM$ map (Figure 1e), collected at an X-ray energy of 284.5 eV, are indeed complementary. These orthogonal energies were determined from NEXAFS spectra of pristine films of both materials. The P3HT nanoparticles and $PC_{61}BM$ nanoparticles could also be distinguished by their different shape and surface texture observed in the SEM images of $P3HT_{NP}$ (Figure 1a), $PC_{61}BM_{NP}$ (Figure 1b), and $P3HT_{NP}$:$PC_{61}BM_{NP}$ (Figure 1c) films. The pristine P3HT nanoparticles are less spherical than pristine $PC_{61}BM$ nanoparticles (Figure 1a,b); possessing a wrinkled texture, which we attribute to the presence of crystalline polymer domains within the nanoparticles (the polymer existing in both crystalline domains and amorphous domains within the nanoparticles). The crystalline ordering of the P3HT in the pristine polymer nanoparticles is confirmed by the presence of vibronic peaks[29] at 560 and 610 nm in the UV−vis absorbance spectra (Figure 2a). The SEM, TEM (Figure 1f), and STXM data all show that a two-phase microstructured film can be generated by combining pristine P3HT nanoparticles with pristine $PC_{61}BM$ nanoparticles and that the two nanoparticle types are evenly mixed throughout the resulting film. This even mixing, or random assembly, can be attributed to the identical surface charge on opposite type particles, making them indistinguishable from the perspective of the particle surface. Organic nanoparticles synthesized via this miniemulsion process will possess a monolayer of surfactant at the solid−air interface (or solid−liquid interface while dispersed in aqueous media), with the polar sulfate groups of sodium dodecyl sulfate molecules located at the particle surface.[11] Further evidence for random assembly of opposite type nanoparticles is provided in Figure S4.

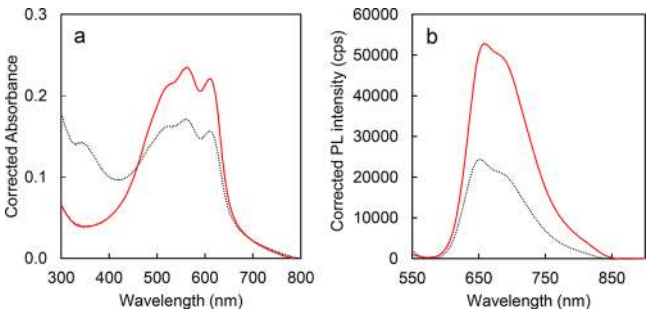

Figure 2. (a) UV−visible absorbance and (b) photoluminescence (PL) spectra of nanoparticle film spin coated from a 1:1 $P3HT_{NP}$:$PC_{61}BM_{NP}$ ink, as cast film (T0) (dotted line). Pristine P3HT nanoparticle film (red line).

UV−vis absorbance and photoluminescence (PL) spectra were recorded on pristine P3HT nanoparticle films and $P3HT_{NP}$:$PC_{61}BM_{NP}$ films (T0) (Figure 2). The UV−vis absorbance spectrum (Figure 2a) of the P3HT nanoparticle film exhibits vibronic peaks characteristic of ordered, crystalline P3HT,[29,30] and the PL spectrum (Figure 2b) exhibits both the 0−0 transition at ∼650 nm and the 0−1 transition at ∼690 nm. The presence of both the 0−0 and 0−1 peaks in the PL spectrum indicates that the P3HT NPs contain both J-aggregates and H-aggregates, representative of both intrachain and interchain ordering, respectively, consistent with the work of Spano[31−33] and Barnes[34] for solvent cast P3HT films. The mini-emulsion nanoparticle fabrication method has previously shown to produce nanoparticles containing crystalline polymer domains for similar studies.[8,35] An excitation wavelength (λ_{exc}) of 500 nm was utilized for PL measurements and, since this wavelength is outside of the peak absorption range of $PC_{61}BM$[36,37] ($PC_{61}BM$ NP UV−vis absorbance spectrum provided in Figure S5), the majority of excitons generated can be assumed to originate in the P3HT nanoparticle domains. When combining $PC_{61}BM$ nanoparticles with the P3HT nanoparticles in a 1:1 ratio ($P3HT_{NP}$:$PC_{61}BM_{NP}$), and spin coating a film, we observed a reduction in the PL emission from P3HT. As observed in the SEM in Figure 1c, the addition of $PC_{61}BM$ nanoparticles leads to the generation of numerous donor−acceptor interfaces for exciton dissociation, where $PC_{61}BM$ nanoparticles neighbor P3HT nanoparticles, hence quenching the PL emission. We calculated the exciton dissociation efficiency (η_{ED}) of the $P3HT_{NP}$:$PC_{61}BM_{NP}$ film from the PL and UV−vis spectra (using eqs 2 and 3 in Experimental Methods) to be 37 ± 2%. Considering that the average nanoparticle size and thus feature size of the two-phase microstructure is 150 nm (P3HT nanoparticles) (Figure S1), an η_{ED} of 37% is remarkably efficient.[38]

Kinetic Monte Carlo (KMC) Simulations. KMC models have been effectively used to elucidate exciton transport mechanisms and associated structure−function relations in OPV devices.[39−41] Here, we apply our KMC model[42] to investigate the remarkably high η_{ED} in the two-phase microstructure. While the KMC approach is ideally suited to investigate the impact of microstructure on PV performance, including η_{ED}, these models are typically based on a virtual microstructure that is not necessarily a true representation of the real microstructure. Uniquely, we have converted SEM micrographs into virtual morphologies, which are a direct input to the KMC model. In this way, a true representation of the two-phase microstructure is created. A 1:1 $P3HT_{NP}$:$PC_{61}BM_{NP}$ film was spin coated onto a quartz glass substrate at the same conditions utilized for preparing films for PL and UV−vis spectroscopy measurements. This $P3HT_{NP}$:$PC_{61}BM_{NP}$ film was then coated with a thin layer of carbon to facilitate SEM imaging

DOI: 10.1021/acs.chemmater.8b03222
Chem. Mater. XXXX, XXX, XXX−XXX

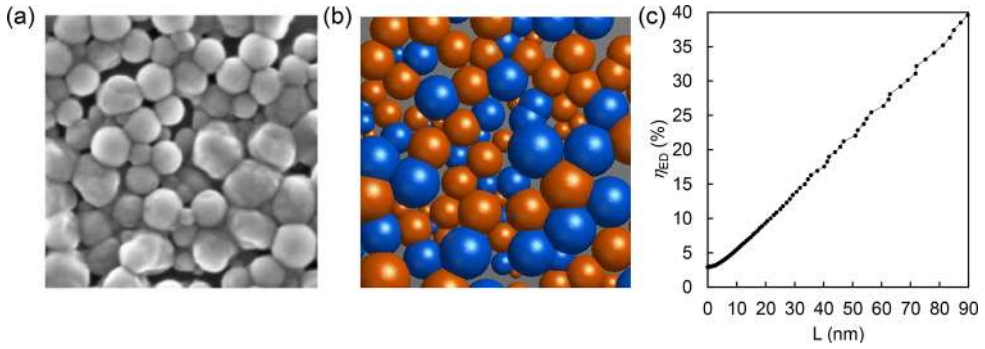

Figure 3. (a) SEM image of a carbon coated 1:1 $P3HT_{NP}$:$PC_{61}BM_{NP}$ film spin coated onto quartz glass, (b) simulated nanoparticle film morphology generated from SEM in panel a, (c) exciton dissociation efficiency (η_{ED}) versus effective displacement of excitons (L) calculated by the KMC model using the simulated $P3HT_{NP}$:$PC_{61}BM_{NP}$ film morphology.

on a nonconductive substrate (quartz glass). Following collection of SEM micrographs, a simulated nanoparticle film morphology (Figure 3b) was generated from a region of the film selected from SEM imaging (Figure 3a) for the particle packing in the film to be reflected. Particle type was then assigned by assuming even mixing as indicated by STXM. Our system consists of a cubic lattice of exciton sites, where each site is either P3HT, $PC_{61}BM$, or empty space, with excitons confined to P3HT and $PC_{61}BM$ sites. To model our film as closely as possible, with its wide range of particle sizes, the morphology was generated directly from an SEM image of the nanoparticle film used for the experimental measurements. Spheres were fitted to the SEM image and the material of each nanoparticle assigned by hand. By superimposing these spheres on our system lattice, sites were assigned P3HT/$PC_{61}BM$ if they were enclosed by a sphere or assigned as empty space otherwise. If a site was within two spheres of different material, it was assigned to the sphere with the nearest center. As the resolution of the SEM and the chromophore size of organic materials are both approximately 3 nm, we chose 3 nm as our lattice spacing. This simulated nanoparticle film morphology (Figure 3b) was directly used for KMC simulations.

For our organic nanoparticle system, four types of event are possible. (i) Generation of an exciton on a P3HT site. As the system was excited at a wavelength outside of the peak absorption range of $PC_{61}BM$, generation on $PC_{61}BM$ sites are not modeled. (ii) Recombination of an exciton with rate $k_{recomb} = 1/\tau$, where τ is the exciton lifetime in the relevant material. (iii) Dissociation of an exciton at a boundary between P3HT and $PC_{61}BM$, with a large rate $k_{dissoc} = 10^{15}$ Hz chosen to make dissociation very likely.[43] (iv) Förster transfer of an exciton from one site to another with rate:

$$k_{FRET} = \frac{1}{\tau}\left(\frac{R_0}{r}\right)^6 \times \begin{cases} 1, & \Delta E \le 0 \\ \exp\left(-\frac{\Delta E}{k_B T}\right), & \Delta E > 0 \end{cases} \quad (1)$$

where r is the distance between the two sites, R_0 the Förster radius between the two materials, and ΔE the change in exciton energy. Both homogeneous (from P3HT sites to other P3HT sites) and heterogeneous (from P3HT to $PC_{61}BM$) energy transfer are allowed and associated hopping rates are calculated using the corresponding Förster radii. The Förster radius for heterogeneous transfer from P3HT to $PC_{61}BM$ was previously determined to be 2.7 nm.[42] At the beginning of each simulation, energies were assigned to each site randomly from a Gaussian distribution with standard deviation 0.06 eV for P3HT and 0.09 eV for $PC_{61}BM$.[42] The energy of each $PC_{61}BM$ site was lower than the energy of each P3HT site so that hopping from the P3HT to the $PC_{61}BM$ was always favorable.

To determine the relation between Förster radius and diffusion length, simulations for a range of Förster radii were initially run for a box of just P3HT with periodic boundaries in all directions. The distance each exciton traveled between generation and recombination was recorded. The diffusion length L was then calculated as the root−mean−square of all the distances traveled.

The diffusion length of excitons in the P3HT phase was systematically increased until the simulated η_{ED} matched the experimentally observed η_{ED} (Figure 3c). The effective displacement of the excitons was found to be 86 nm, which corresponds to a 1D exciton diffusion length of 50 nm. This value is about five-times larger than the expected exciton diffusion length in P3HT.[43,44] UV−vis spectra of P3HT nanoparticles show particularly pronounced vibronic structure, which is indicative of large or many crystalline P3HT domains. Such crystallinity allows for exciton delocalization over larger regions.[45] This increased delocalization of excitons in the nanoparticle structure is thought to be the reason for the large exciton displacement and resulting fluorescence quenching. Such an effect was previously identified and modeled using a combined delocalization and diffusion scheme.[46] Indeed, many crystalline organic semiconductors exhibit large exciton displacement capability.[40,47,48] The observed large exciton displacement shows that the mini-emulsion method produces P3HT particles with a promising microstructure for efficient exciton dissociation. Further enhancement of the η_{ED} is obtained by introducing a third intermixed donor−acceptor phase.

Thin Film Morphology: Three-Phase Microstructure. To generate first a continuous solid film from the deposited nanoparticles, and second a third intermixed donor−acceptor phase, the materials are heated to a temperature above the T_g of both components to facilitate softening and interdiffusion. Numerous studies have shown that the polymer T_g is critical to the interdiffusion of fullerene and polymer.[49,50] This annealing process essentially connects the nanodomains to (1) create continuous pathways for charge transport to the electrodes and (2) increase exciton dissociation efficiency by increasing donor−acceptor interfacial area. The T_g of both pristine P3HT nanoparticles and pristine $PC_{61}BM$ nanoparticles were determined using dynamic mechanical thermal analysis (DMTA), a technique often applied to thin polymer films.[51] The P3HT nanoparticles and $PC_{61}BM$ nanoparticles were drop

DOI: 10.1021/acs.chemmater.8b03222
Chem. Mater. XXXX, XXX, XXX−XXX

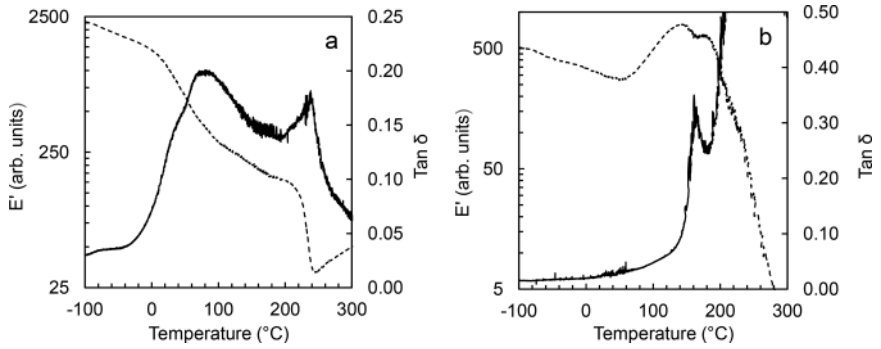

Figure 4. Dynamic mechanical thermal analysis (DMTA) temperature scans of (a) pristine P3HT nanoparticles and (b) pristine $PC_{61}BM$ nanoparticles drop cast onto a glass fiber mesh. Storage modulus (E') (dashed line) and tan δ (solid line) are presented.

cast onto a woven glass fiber mesh and allowed to air-dry to obtain reinforced films. A sinusoidal stress was applied to each sample, with a frequency of 1 Hz and an amplitude of 5 μm, the sample temperature was increased at a rate of 3 °C/min to a temperature of 300 °C and the phase lag monitored as an indicator of the change in the sample's elastic properties. Consistent with Sharma et al.[51] we observe two tan δ peaks in the temperature range of 20 to 100 °C in Figure 4a (accompanied by a significant storage modulus, E', drop), with the first peak at 38 °C manifesting as a shoulder on the second peak at 80 °C (Table 1). As such, we can assign the peak at 38 °C to the T_g of the P3HT nanoparticles, in agreement with previous DMTA studies of P3HT.[51] Specifically, we propose the 38 °C peak represents the mobile amorphous P3HT fraction (MAF) and the 80 °C peak represents the relaxation of the rigid amorphous P3HT fraction (RAF), where the RAF exists at the boundaries of the crystalline P3HT domains and hence its movement is hindered by these crystals, consistent with the definitions of Martín et al.[52] While Sharma et al.[51] assigned the 38 °C tan δ peak in the pure polymer sample scan as a T_g, they did not assign the tan δ peak observed at ~90 °C. However, from the more recent report of Martín et al.,[52] it is evident that this second peak in the pure polymer sample can be assigned to the RAF. Hence, here we compare the ratio of the lower temperature MAF peak to the higher temperature RAF peak for a solvent cast P3HT film, as measured by Sharma et al.,[51] to that of the highly crystalline P3HT NP film, as measured in our present study. The ratio of the 38 °C peak to the 80 °C peak observed for pristine P3HT NPs in Figure 4a is lower than that reported in Sharma et

Table 1. Glass Transition Temperature (T_g) Derived from DMTA Measurements for Single Component Nanoparticles

nanoparticle type	polymer fraction classification	T_g (°C)
$P3HT_{NP}$	MAF	38
	RAF	80
$PC_{61}BM_{NP}$		161

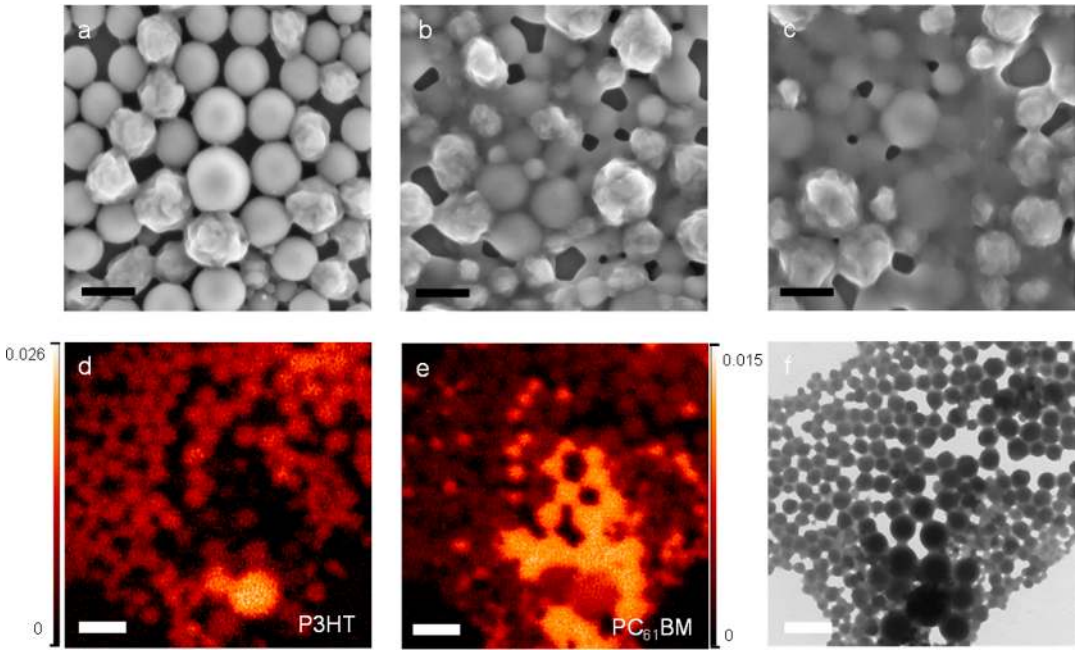

Figure 5. SEM image of $P3HT_{NP}$:$PC_{61}BM_{NP}$ film (a) dried at 110 °C 4 min (T1), (b) dried at 110 °C 4 min followed by annealing at 140 °C 4 min (T2), and (c) dried at 110 °C 4 min followed by annealing at 140 °C 10 min (T3) (scale bars are 200 nm in panels a–c). STXM mass plots showing concentration of (d) P3HT and (e) $PC_{61}BM$ in a $P3HT_{NP}$:$PC_{61}BM_{NP}$ film thermally treated at 110 °C 4 min followed by annealing at 140 °C for 10 min (T3) (scale bars are 600 nm in panels d and e). The color scale bars indicate concentration of component in mg/cm^2. (f) Position-matched TEM image for the thermally treated $P3HT_{NP}$:$PC_{61}BM_{NP}$ film in panels d and e. Scale bar in panel f is 600 nm.

DOI: 10.1021/acs.chemmater.8b03222
Chem. Mater. XXXX, XXX, XXX−XXX

al.[51] for a solvent cast P3HT film, which is due to the comparatively high fraction of crystalline P3HT in our nanoparticulate system and hence high fraction of associated RAF. For the $PC_{61}BM$ nanoparticles we observe a tan δ peak at 161 °C, which we assign to the material T_g (Figure 4b), consistent with previous reports of the T_g of $PC_{61}BM$ determined from a combination of methods, including grazing-angle X-ray scattering, variable-temperature ellipsometry, and differential scanning calorimetry.[50]

Thermal treatment of the $P3HT_{NP}$:$PC_{61}BM_{NP}$ film was in three stages and the temperature was matched to the drying and annealing conditions reported in the literature for NP OPV.[8,24] SEM measurements were performed on a $P3HT_{NP}$:$PC_{61}BM_{NP}$ film exposed to (i) a drying treatment of 110 °C for 4 min (T1) (Figure 5a), (ii) a drying treatment of 110 °C for 4 min followed by an annealing treatment of 140 °C for 4 min (T2) (Figure 5b), and (iii) a drying treatment of 110 °C for 4 min followed by an annealing treatment of 140 °C for 10 min (T3) (Figure 5c). The nanoparticles progressively sintered together through these three stages of thermal treatment, as observed in the SEM images. STXM composition maps were collected, together with position-matched TEM images, for a $P3HT_{NP}$:$PC_{61}BM_{NP}$ film exposed to a drying treatment of 110 °C 4 min followed by an annealing treatment of 140 °C 10 min (Figure 5d–f). The composition analysis of the P3HT nanoparticles following thermal treatment gave a value of 72–80% P3HT and 20–28% $PC_{61}BM$, indicating the diffusion of $PC_{61}BM$ from neighboring $PC_{61}BM$ nanoparticles into the P3HT nanoparticles. Although the P3HT nanoparticles are initially composed of numerous subdomains of crystalline and amorphous P3HT, the diffusion of $PC_{61}BM$ into P3HT requires pathways of amorphous P3HT.[12,53,54] As such, the local concentration of $PC_{61}BM$ in the amorphous P3HT domains will actually be higher than 20–28% since the subdomains are below the STXM resolution limit and thus the measured composition is an average over the entire nanoparticle.

We here note that there is void space evident in the STXM, TEM and SEM micrographs in Figure 5, which is not ideal for effective charge transport in an OPV photoactive layer. The film deposition conditions utilized for preparation of these films were selected for generation of monolayers for ease of imaging. Modifying the film deposition conditions can easily lead to denser particle packing, for example, by increasing the ink solids loading and lowering the coating speed.

The $P3HT_{NP}$:$PC_{61}BM_{NP}$ film was exposed to a series of annealing treatments and after each treatment a PL emission spectrum and a UV–vis absorbance spectrum were collected (Figure 6). When the same $P3HT_{NP}$:$PC_{61}BM_{NP}$ film (measured in Figure 2) is thermally treated at 110 °C for 4 min (T1) we observe some PL quenching, followed by further PL quenching for a thermal treatment of 140 °C 4 min (T2). This increase in PL quenching (accompanied by an unmodified absorbance) is indicative of an increase in the interfacial area between donor and acceptor material domains, which can occur via two processes: (1) softening of nanoparticles and increased surface area of contact between dissimilar nanoparticles (observed in SEM images in Figure 5a–c), (2) $PC_{61}BM$ diffusion into neighboring P3HT nanoparticles (observed in STXM in Figure 5e). The η_{ED} was calculated for the $P3HT_{NP}$:$PC_{61}BM_{NP}$ film exposed to the series of thermal annealing treatments T1 to T3 and presented in Table 2. The η_{ED} for the $P3HT_{NP}$:$PC_{61}BM_{NP}$ film exposed to 110 °C 4 min (T1) was calculated to be 60 ± 2%, a large increase from that of the untreated $P3HT_{NP}$:$PC_{61}BM_{NP}$ film (T0) (η_{ED} = 37 ± 2%). The η_{ED} then further increases to 63 ± 1% following the 140 °C 4 min thermal treatment (T2). The third thermal treatment (140 °C 10 min) (T3) shows only a very minor decrease in PL intensity compared to the 140 °C 4 min treatment and an increase in η_{ED} to 64 ± 1%, indicating that the majority of $PC_{61}BM$ diffusion into the neighboring P3HT amorphous phases occurs earlier. Importantly, for the 140 °C 10 min treated sample we still observe a PL signal that can be attributed to the semicrystalline P3HT domains in the P3HT nanoparticles, into which $PC_{61}BM$ will not diffuse.[12,14] The vibronic peaks in the UV–vis absorbance spectra (characteristic of crystalline P3HT) also remain unchanged throughout the annealing series (Figure 6a), confirming that any interdiffusion occurs without the disruption of crystalline P3HT domains, as reported previously for solvent-cast bilayer systems.[12,54] Also, the 0–0/0–1 intensity ratio in the PL spectra varies little following thermal annealing treatments of the $P3HT_{NP}$:$PC_{61}BM_{NP}$ film (3% variation), indicating little change in the ratio of J-type to H-type aggregates in the P3HT NPs. The $PC_{61}BM$ diffusion occurs through the amorphous P3HT phase, such as at the grain boundaries between the ordered, crystalline P3HT.[54] Yin et al.[14] measured the size of such ordered, crystalline P3HT domains to be 120 to 150 Å in a pristine P3HT film via neutron scattering. Regarding the PL quenching observed following the 110 °C 4 min thermal treatment, this temperature is above the T_g of the polymer but below the T_g of $PC_{61}BM$. We propose a small amount of $PC_{61}BM$ diffusion has occurred just below its T_g, Treat et al.[55] showed that disordered $PC_{61}BM$ readily diffuses into disordered P3HT at 110 °C. This diffusion of $PC_{61}BM$ likely forms a blended interfacial region between the P3HT nanoparticles and $PC_{61}BM$ nanoparticles in the film as well as within the amorphous P3HT subdomains existing within the semicrystalline P3HT nanoparticles.

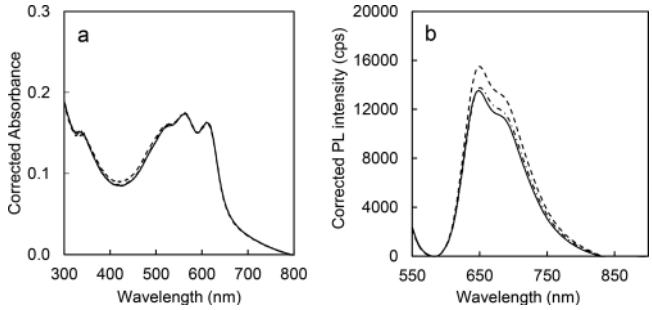

Figure 6. (a) UV–visible absorbance and (b) photoluminescence spectra of nanoparticle films spin coated from a 1:1 $P3HT_{NP}$:$PC_{61}BM_{NP}$ ink and thermally treated. $P3HT_{NP}$:$PC_{61}BM_{NP}$ film dried at 110 °C 4 min (T1) (dashed line); dried at 110 °C 4 min and annealed at 140 °C 4 min (T2) (dot-dashed line); and dried at 110 °C 4 min and annealed at 140 °C 10 min (T3) (solid line).

Table 2. Experimentally Calculated Exciton Dissociation Efficiency (η_{ED}) (Average and Standard Deviation) of $P3HT_{NP}$:$PC_{61}BM_{NP}$ Film Exposed to Thermal Annealing Conditions T1 to T3[a]

thermal annealing condition	110 °C treatment time (min)	140 °C treatment time (min)	η_{ED} (%)	σ (%)
T0			37	2
T1	4		60	2
T2	4	4	63	1
T3	4	10	64	1

[a]T0 is no thermal annealing treatment.

DOI: 10.1021/acs.chemmater.8b03222
Chem. Mater. XXXX, XXX, XXX–XXX

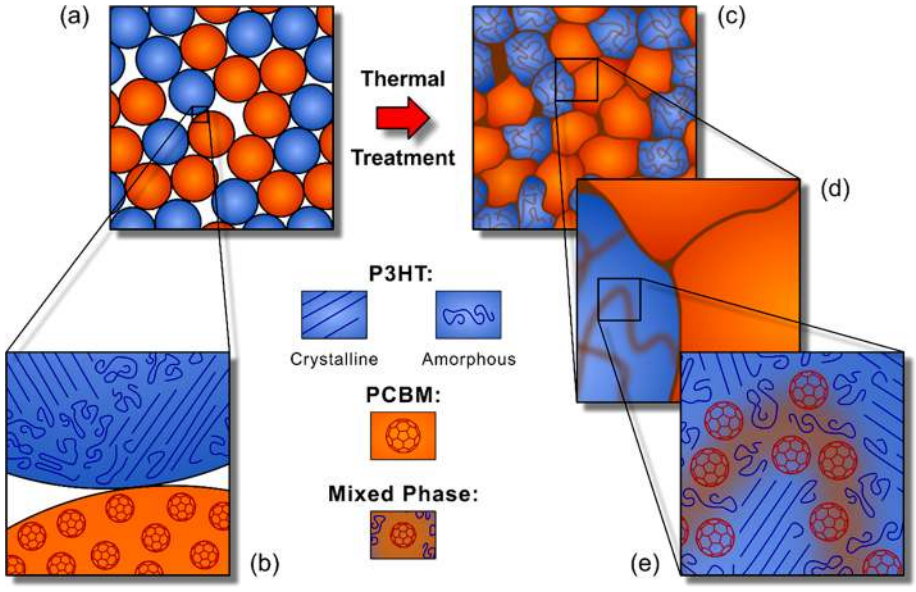

Figure 7. Schematic depicting the conceptual model of the evolution in thin film morphology. (a) Two-phase film microstructure generated from colloidal nanoparticle inks, (b) composition of neighboring opposite-type nanoparticles (with the P3HT nanoparticles comprising crystalline P3HT and amorphous P3HT subdomains). Three-phase film microstructure generated from thermally annealing the two-phase film, (c) sintering of nanoparticles to form a continuous film and (d, e) formation of a third intermixed phase.

The change in nanoparticle film structure from a two-phase system to a three-phase system can be likened to existing polymer:fullerene bilayer film studies,[12,13,49,54,56] which show that when an initial sample consisting of material pure layers of donor and acceptor is thermally annealed one layer will swell due to diffusion of material from the other layer. Collins et al.[17] showed that even short annealing times cause significant interdiffusion in P3HT:$PC_{61}BM$ bilayers, demonstrating that under no conditions do pure amorphous P3HT phases exist in BHJ or annealed bilayer devices. Chen et al.[54] showed that the diffusion of $PC_{61}BM$ into P3HT is almost ballistic in nature, with $PC_{61}BM$ completely diffusing through a 100 nm P3HT layer in the first 5 s of annealing at 150 °C. These studies showed that within amorphous P3HT regions, pure phases are not thermodynamically favored. Hence, we propose the annealing applied in our nanoparticle study is sufficient to generate a three-phase microstructure when beginning with pristine P3HT nanoparticles and pristine $PC_{61}BM$ nanoparticles.

Several studies have reported the formation and composition of molecularly mixed phases in solvent cast BHJ and bilayer films. He et al.[57] patterned a $PC_{61}BM$ film on silicon nitride using photolithography, then deposited a P3HT film onto the patterned $PC_{61}BM$ film and annealed the bilayer structure to study the lateral intermixing and facilitate measurement of fullerene miscibility. The composition measurements were made with NEXAFS and STXM. The authors observed a 20% miscibility of $PC_{61}BM$ in regiorandom (RRa) P3HT, and a lower value for regioregular (RR) P3HT (2.8 to 10.8%). Lee et al.[56] reported a higher value of 35% for the miscibility of $PC_{61}BM$ in P3HT using neutron reflectometry in combination with X-ray photoelectron spectroscopy (XPS). Wang et al.[58] studied the diffusion of $PC_{71}BM$ into the low band gap polymer PTB7 for a bilayer sample structure; notably PTB7 has a much lower crystallinity than P3HT. A majority fraction of disordered PTB7 enabled continuous paths for $PC_{71}BM$ diffusion, with the diffusion front mapped using nanomechanical AFM and GI XRD.

The two processes leading to the increase in η_{ED} upon applying thermal treatments to the nanoparticle film are illustrated in Figure 7. Softening of the nanoparticles (Process 1) leads to an increase in contact surface area between pristine P3HT and pristine $PC_{61}BM$ nanoparticles as the particles sinter together. In contrast, diffusion of $PC_{61}BM$ from the $PC_{61}BM$ nanoparticles into the amorphous P3HT fraction of the P3HT nanoparticles (Process 2) generates of a third material phase consisting of molecularly mixed P3HT:$PC_{61}BM$.

Outlook for Engineering Photoactive Layer Morphologies. When considering a BHJ film cast from a solution of polymer and fullerene, the structure of the resulting film is determined by a complex interplay of multiple processes, namely the thermodynamics of demixing and phase separation, and the kinetics of nucleation, diffusion, and crystallization. These processes ultimately lead to kinetically trapped morphologies.[58] In this present study, we have demonstrated how to remove the complexity from the morphology optimization process by presetting the donor and acceptor material domain size and composition prior to film deposition (via the nanoparticle route), hence decoupling morphology optimization from film deposition. We have hereby highlighted how it is possible to engineer a three-phase microstructure with phases designed for (a) exciton dissociation (intermixed phase), (b) hole transport (pure crystalline polymer phase), and (c) electron transport (pure fullerene phase) by utilization of organic nanoparticle colloidal inks. With the benefit of this route being eco-friendly fabrication from water-based dispersions. Annealing treatments applied to the pristine donor nanoparticle/pristine acceptor nanoparticle films effectively sintered the nanoparticles together and also led to the generation of the third intermixed phase. This interdiffusion is in contrast to the demixing previously reported for P3HT:$PC_{61}BM$ core−shell nanoparticle films.[8,23] The pristine nanoparticle route potentially offers a superior route to tailoring optimal photoactive layer structures and can be applied to a range of donor and acceptor semiconducting materials.

DOI: 10.1021/acs.chemmater.8b03222
Chem. Mater. XXXX, XXX, XXX−XXX

CONCLUSIONS

Here we have shown that the pristine particle route offers a number of advantages for engineering photoactive layer morphologies. We have demonstrated the capability for engineering two-phase and three-phase donor−acceptor morphologies, generating phases designed for exciton dissociation (molecularly mixed phase), as well as phases designed for hole transport (crystalline P3HT pure phase) and electron transport ($PC_{61}BM$ pure phase). The photoactive layer morphologies are achieved with eco-friendly water-based colloidal inks. STXM and PL quenching data indicated the diffusion of $PC_{61}BM$ into neighboring P3HT nanoparticles upon annealing, generating the intermixed third phase. The nanoscopic kinetic Monte Carlo model developed in this work has been instrumental in enabling us to assess exciton transport properties that are experimentally inaccessible in these complex multiphase material systems. This work is paving the way for achieving OPV photoactive layers with targeted pure bicontinuous percolation pathways, and a third intermixed phase for improved exciton dissociation, from water-based printing inks. The pristine nanoparticle route shows that nanostructured film morphologies can be attained with a superior level of control than previously reported core−shell nanoparticles.

EXPERIMENTAL METHODS

Materials. $PC_{61}BM$ was purchased from Solenne BV (Netherlands). Anhydrous chloroform and sodium dodecyl sulfate (SDS) were purchased from Sigma-Aldrich. P3HT was synthesized as described by Holmes et al.[23] The molecular weight and PDI of P3HT were measured on a Waters GPC 1515 pump system equipped with Empower software (at ANFF-Q). The instrument was equipped with refractive index, ultraviolet and Shimadzu multiangle light scattering detectors. The running solvent was tetrahydrofuran (THF), the column temperature was 40 °C, and the flow rate was 1 mL/min. Polymer solutions were prepared at a concentration of 1 mg/mL (THF) and prefiltered through 0.45 μm PTFE (poly(tetrafluoroethylene)) filters. Two types of columns (Styragel HT-6E and Styragel HT-3) were used to analyze the polymer samples. Polystyrene narrow standards (range: 1.35×10^3−1.3×10^6 g mol^{-1}) were used to create a molecular weight calibration curve. The molecular weight of P3HT was calculated tobe M_n 16 770 g mol^{-1}, M_w 22 270 g mol^{-1}, PDI 1.33. The P3HT regioregularity was 95%, calculated from ^{1}H NMR spectra using the method reported by Iovu et al.[59]

Nanoparticle Synthesis. The mini-emulsion organic phase ("oil" phase) was prepared by dissolving either 30 mg of P3HT or 30 mg of $PC_{61}BM$ in 1.08 mL chloroform. The mini-emulsion aqueous phase was prepared by dissolving 1 mg of SDS surfactant in 2.8 mL of Milli-Q filtered water. The surfactant concentration was purposely low so as to achieve a broad distribution in nanoparticle sizes for STXM imaging. Macroemulsions were generated by combining the organic and aqueous phases and stirring at 1100 rpm, 33 °C for 1 h. A mini-emulsion was generated using ultrasonication via a Hielscher UP400S ultrasonic processor with a 7 mm diameter tip. Sonication was for 2 min at 25 W and an amplitude setting of 40%, an ice bath was used to prevent overheating of the sample. Following sonication, the mini-emulsion was transferred immediately to a hot plate for chloroform solvent evaporation at 60 °C with rapid stirring. This evaporation was performed for a minimum of 3 h to ensure complete removal of chloroform. Importantly, in future large-scale nanoparticle fabrication, the volatile organic solvent that is required in the initial fabrication step can be reused in a closed synthesis cycle. Centrifugal dialysis was used to reduce the total volume of the nanoparticle inks to 0.5 mL.

NEXAFS. NEXAFS provides a fingerprint spectrum that is unique to each component of a blend system[60] by probing the element-specific excitations of core electrons to unoccupied molecular orbitals.[61] NEXAFS at the C K-edge has been utilized for the measurement of conjugated polymers and fullerene molecules in this study. Pristine films of P3HT and $PC_{61}BM$ were spin coated from chloroform solutions onto PEDOT:PSS coated glass substrates, floated off onto water, and mounted on copper grids for NEXAFS measurements. NEXAFS spectra were normalized to film thickness before the singular value decomposition (SVD) fitting routine (associated with STXM analysis) was performed. From the NEXAFS spectra of P3HT and $PC_{61}BM$, an energy of 284.5 eV was chosen as the key absorption energy for $PC_{61}BM$ and an energy of 285.3 eV was chosen as the key absorption energy for P3HT for subsequent STXM measurements. For $PC_{61}BM$, the key absorption peak at 284.5 eV in the NEXAFS spectrum is the characteristic C = C π^* resonance peak, corresponding to a 1s → LUMO transition by a core electron from the fullerene or phenyl carbon atoms.[61]

Microscopy. Samples were prepared for STXM by spin coating 2.5 μL of nanoparticle dispersion/ink onto low stress silicon nitride (Si_3N_4) windows with silicon dioxide coating (window dimensions 0.25×0.25 mm^2, window thickness 15 nm, frame 5×5 mm^2) (purchased from Norcada, Canada) at 3000 rpm, 1 min, low acceleration of 112 rpm/s. Unannealed (or "as cast") samples were air-dried. Thermally dried samples were placed on a hot plate at 110 °C for 4 min. Thermally annealed samples were placed on a hot plate at 140 °C for either 4 or 10 min. STXM measurements were performed on beamline 5.3.2.2 at the Advanced Light Source.[62] The samples deposited on Si_3N_4 were mounted in the sample chamber, which was backfilled with helium (0.33 atm), and rastered with respect to the X-ray beam. The transmitted X-ray beam is detected by a scintillator and a PMT. The energy of the X-ray beam was varied between 270 and 340 eV, covering the C K-edge region at a resolution of 0.1 eV. Image analysis was performed with the aXis2000 package (http://unicorn.mcmaster.ca/aXis2000.html). Further details of STXM experimental methods and data analysis methods can be found in the literature.[63]

The Si_3N_4 substrates with deposited nanoparticles were transported back to the University of Newcastle (Australia) where transmission electron microscopy (TEM) was used to reimage the same particles for collecting position-matched images. TEM was performed on a Jeol 1200 EXII at an accelerating voltage of 80 kV at varying magnification ranges.

Samples were prepared for SEM by spin coating 2.5 μL of the nanoparticle dispersion/ink (3000 rpm, 1 min, low acceleration of 112 rpm/s) onto a conductive silicon substrate. SEM was performed on a Leo Gemini 1530 SEM (Figures 1 and 5) and a Zeiss Sigma VP FESEM (for generation of a simulated morphology for KMC), both operating at an accelerating voltage of 2 kV.

For the KMC study, a 1:1 $P3HT_{NP}$:$PC_{61}BM_{NP}$ film was spin coated onto a quartz glass substrate to match the preparation conditions of the film used for PL and UV−vis spectroscopy measurement, a thin carbon coating (24 nm) was applied to the $P3HT_{NP}$:$PC_{61}BM_{NP}$ film using a Cressington 208 Carbon Coater before SEM imaging.

UV−vis and PL Spectroscopy. Initial steady-state fluorescence spectra were measured on a SPEX FL3−11 TAU fluorimeter, purchased from GammaData, Sweden. Measurements were performed in the right-angle mode at 55° angle, relative to the incident excitation light. The excitation wavelength was λ_{ex} = 410 nm. The excitation wavelength was chosen from UV/vis absorption measurements of P3HT. To avoid scattering of the excitation light, a 425 nm high-pass cutoff filter from Edmund Optics was placed between the sample and the detector. All spectra were recorded at room temperature. These measurements formed the preliminary investigation.

For collecting data sets for the calculation of experimental η_{ED} (data presented in Figures 2 and 6), PL and UV−vis studies were performed on a 1:1 $P3HT_{NP}$:$PC_{61}BM_{NP}$ film exposed to various annealing treatments. The following describes these experimental measurements. Fluorescence spectra were measured on a Shimadzu RF-6000 fluorimeter with a beam to sample angle of 65 degrees, λ_{exc} = 500 nm, λ_{em} = 550−900 nm, excitation bandwidth = 20 nm, emission bandwidth = 20 nm. A 420 nm high-pass cutoff filter was placed in the beam path before the sample. The experimental exciton dissociation efficiency (η_{ED}) was calculated using eqs 2 and 3. The PL spectra were

DOI: 10.1021/acs.chemmater.8b03222
Chem. Mater. XXXX, XXX, XXX−XXX

first normalized to PL intensity at 900 nm. The units of the PL signal were then converted via the equation $E = hc/\lambda$ at each point in the spectrum. This conversion was performed to obtain a plot representative of the number of photons emitted, which is directly proportional to the number of unquenched excitons. The spectrum was then integrated between λ = 850 and 600 nm, this value was then divided by the absorption of the film at 500 nm (%A_{500}) (eq 2). The %A_{500} value was taken following normalizing the UV−vis absorbance spectra (background subtraction at 800 nm). For the P3HT$_{NP}$:PC$_{61}$BM$_{NP}$ film, the contribution of PC$_{61}$BM to blend film absorption at 500 nm was subtracted prior to calculation of PL$_C$. The photoluminescence of the mixed P3HT$_{NP}$:PC$_{61}$BM$_{NP}$ film (PL_c^{MP}) was then normalized to the photoluminescence of pristine P3HT nanoparticles (PL_c^{P3HT}), subtracting this value from one gave the η_{ED} (eq 3). In general, a proportion of the additional PL quenching due to the presence of PC$_{61}$BM$_{NP}$ can be ascribed to heterogeneous energy transfer from P3HT to PC$_{61}$BM. However, such energy transfer is followed by exciton dissociation.[64] We have previously shown that if the electron and hole transfer efficiencies across the donor:acceptor interface is similar, the same η_{ED} is obtained regardless of whether heterogeneous energy transfer is taken into account.[42] Given that for the P3HT:PC$_{61}$BM system both electron and hole transfer is near 100%,[42] heterogeneous energy transfer can be ignored when calculating the experimental η_{ED}. The average η_{ED} ± standard deviation for replicate measurements of each film is provided and also in table format in Table 2:

$$PL_c = \frac{\int_{\lambda=600}^{\lambda=850} [PL(\lambda) - PL(900)]\, d\lambda}{\%A_{500}} \quad (2)$$

$$\eta_{ED} = 1 - \frac{PL_c^{MP}}{PL_c^{P3HT}} \quad (3)$$

UV−vis measurements were taken using an ultraviolet−visible absorption spectrophotometer (UV−vis, Varian Cary 6000i) in the wavelength range 300−800 nm.

KMC Method. The kinetic Monte Carlo (KMC) algorithm is a method for modeling how a physical system evolves over time. KMC differs from some other Monte Carlo methods in that the trajectories of individual particles are explicitly modeled and tracked. This makes it a useful tool in determining the exciton dissociation efficiency (η_{ED}) of our organic systems, as the number of excitons that dissociate and recombine can be counted. The progression of the system is accomplished by modeling every process that can occur as a discrete event with rate r_i. Each step, all rates are calculated and an event i picked at random with a probability $p_i = r_i/\Sigma_j r_j$ where $\Sigma_j r_j$ is the sum of rates of all processes in the system. The system time is then incremented by $-\ln(u)/\Sigma_j r_j$ where u is a random number in the range (0, 1]. The $-\ln(u)$ term draws a time from a uniform Poisson distribution which is then normalized to the correct time scale by the sum of rates term. The simulation progresses until a predetermined amount of time has elapsed, here 1 ms.

Thermomechanical Analysis. Dynamic mechanical thermal analysis (DMTA) was performed on a TA Q800 DMA in strain-controlled mode with a frequency of 1 Hz, amplitude of 5 μm, temperature ramp of 3 °C/min, temperature range of −110 to 300 °C, and under a nitrogen environment (60 mmHg). The first scan was run from room temperature to 30 °C to remove possible moisture from the samples. Samples were prepared for DMTA by drop-casting nanoparticle inks onto glass fiber mesh substrates cut at a 45° angle toward the grain. Tan $\delta = E''/E'$ where E' is the storage modulus and E'' is the loss modulus. Generally the experimental setup was in accordance with that reported by Sharma et al.[51]

■ ASSOCIATED CONTENT

Supporting Information

The Supporting Information is available free of charge on the ACS Publications website at DOI: 10.1021/acs.chemmater.8b03222.

Nanoparticle size analysis; nanoparticle size variation study; nanoparticle packing analysis; SEM depicting random assembly of P3HT$_{NP}$:PC$_{61}$BM$_{NP}$ film; PC$_{61}$BM$_{NP}$ characterization (PDF)

■ AUTHOR INFORMATION

Corresponding Author

*E-mail: Natalie.Holmes@newcastle.edu.au.

ORCID

Natalie P. Holmes: 0000-0002-8860-7098
Anirudh Sharma: 0000-0003-4841-0108
Mats R. Andersson: 0000-0002-7928-8216
Jan van Stam: 0000-0002-0995-3823
Alison B. Walker: 0000-0002-2232-9734

Author Contributions

▲These authors contributed equally.

Notes

The authors declare no competing financial interest.

■ ACKNOWLEDGMENTS

We acknowledge the support from the Faculty of Health, Science and Engineering of Karlstad University for the mobility grant for N.P.H. as an incoming visiting researcher. The ALS is supported by the Director, Office of Science, Office of Basic Energy Sciences, of the U.S. Department of Energy under Contract No. DE-AC02-05CH11231. We acknowledge financial support from the Commonwealth of Australia through the Access to Major Research Facilities Program. A.B.W. and J.M.C. thank UK EPSRC Supersolar Hub Extension EP/P02484X/1 and EPSRC Centre for Doctoral Training in New and Sustainable PV EP/L01551X/1. This work was performed in part at the Materials node (Newcastle) and the Queensland node of the Australian National Fabrication Facility (ANFF), which is a company established under the National Collaborative Research Infrastructure Strategy to provide nano- and microfabrication facilities for Australia's researchers. Thank you to C. Müller for helpful scientific discussion. Thank you to the University of Newcastle Electron Microscopy and X-ray Unit.

■ ABBREVIATIONS

BHJ, bulk heterojunction; DMTA, dynamic mechanical thermal analysis; KMC, kinetic Monte Carlo; NEXAFS, near edge X-ray absorption fine structure; P3HT, poly(3-hexylthiophene); PC$_{61}$BM, phenyl C$_{61}$ butyric acid methyl ester; PL, photoluminescence; SDS, sodium dodecyl sulfate; SEM, scanning electron microscopy; STXM, scanning transmission X-ray microscopy; TEM, transmission electron microscopy; T_g, glass transition temperature

■ REFERENCES

(1) Tan, L.; Li, P.; Zhang, Q.; Izquierdo, R.; Chaker, M.; Ma, D. Towards Enhancing Solar Cell Performance: An Effective and "Green" Additive. *ACS Appl. Mater. Interfaces* **2018**, *10*, 6498−6504.

(2) Gu, X.; Zhou, Y.; Gu, K.; Kurosawa, T.; Guo, Y.; Li, Y.; Lin, H.; Schroeder, B. C.; Yan, H.; Molina-Lopez, F.; et al. Roll-to-Roll Printed Large-Area All-Polymer Solar Cells with 5% Efficiency Based on a Low

DOI: 10.1021/acs.chemmater.8b03222
Chem. Mater. XXXX, XXX, XXX−XXX

Crystallinity Conjugated Polymer Blend. *Adv. Energy Mater.* **2017**, *7*, 1602742.
(3) Andersen, T. R.; Cooling, N. A.; Almyahi, F.; Hart, A. S.; Nicolaidis, N. C.; Feron, K.; Noori, M.; Vaughan, B.; Griffith, M. J.; Belcher, W. J.; et al. Fully Roll-to-Roll Prepared Organic Solar Cells in Normal Geometry with a Sputter-Coated Aluminium Top-Electrode. *Sol. Energy Mater. Sol. Cells* **2016**, *149*, 103−109.
(4) Duan, C.; Cai, W.; Hsu, B. B. Y.; Zhong, C.; Zhang, K.; Liu, C.; Hu, Z.; Huang, F.; Bazan, G. C.; Heeger, A. J.; et al. Toward Green Solvent Processable Photovoltaic Materials for Polymer Solar Cells: The Role of Highly Polar Pendant Groups in Charge Carrier Transport and Photovoltaic Behavior. *Energy Environ. Sci.* **2013**, *6*, 3022−3034.
(5) Oosterhout, S. D.; Savikhin, V.; Burgers, M. A.; Zhang, J.; Zhang, Y.; Marder, S. R.; Bazan, G. C.; Toney, M. F. Absence of Mixed Phase in Organic Photovoltaic Active Layers Facilitates Use of Green Solvent Processing. *J. Phys. Chem. C* **2018**, *122*, 11136−11144.
(6) Andersen, T. R.; Larsen-Olsen, T. T.; Andreasen, B.; Böttiger, A. P. L.; Carlé, J. E.; Helgesen, M.; Bundgaard, E.; Norrman, K.; Andreasen, J. W.; Jørgensen, M.; et al. Aqueous Processing of Low-Band-Gap Polymer Solar Cells Using Roll-to-Roll Methods. *ACS Nano* **2011**, *5*, 4188−4196.
(7) Nan, Y.-X.; Hu, X.-L.; Larsen-Olsen, T. T.; Andreasen, B.; Tromholt, T.; Andreasen, J. W.; Tanenbaum, D. M.; Chen, H.-Z.; Krebs, F. C. Generation of Native polythiophene/PCBM Composite Nanoparticles via the Combination of Ultrasonic Micronization of Droplets and Thermocleaving from Aqueous Dispersion. *Nanotechnology* **2011**, *22*, 475301.
(8) Holmes, N. P.; Ulum, S.; Sista, P.; Burke, K. B.; Wilson, M. G.; Stefan, M. C.; Zhou, X.; Dastoor, P. C.; Belcher, W. J. The Effect of Polymer Molecular Weight on P3HT:PCBM Nanoparticulate Organic Photovoltaic Device Performance. *Sol. Energy Mater. Sol. Cells* **2014**, *128*, 369−377.
(9) Bag, M.; Gehan, T. S.; Renna, L. a.; Algaier, D. D.; Lahti, P. M.; Venkataraman, D. Fabrication Conditions for Efficient Organic Photovoltaic Cells from Aqueous Dispersions of Nanoparticles. *RSC Adv.* **2014**, *4*, 45325−45331.
(10) Holmes, N. P.; Marks, M.; Kumar, P.; Kroon, R.; Barr, M. G.; Nicolaidis, N.; Feron, K.; Pivrikas, A.; Fahy, A.; Mendaza, A. D. D. Z.; et al. Nano-Pathways: Bridging the Divide between Water-Processable Nanoparticulate and Bulk Heterojunction Organic Photovoltaics. *Nano Energy* **2016**, *19*, 495−510.
(11) Colberts, F. J. M.; Wienk, M. M.; Janssen, R. A. J. Aqueous Nanoparticle Polymer Solar Cells: Effects of Surfactant Concentration and Processing on Device Performance. *ACS Appl. Mater. Interfaces* **2017**, *9*, 13380−13389.
(12) Treat, N. D.; Brady, M. A.; Smith, G.; Toney, M. F.; Kramer, E. J.; Hawker, C. J.; Chabinyc, M. L. Interdiffusion of PCBM and P3HT Reveals Miscibility in a Photovoltaically Active Blend. *Adv. Energy Mater.* **2011**, *1*, 82−89.
(13) Chen, H.; Hu, S.; Zang, H.; Hu, B.; Dadmun, M. Precise Structural Development and Its Correlation to Function in Conjugated Polymer: Fullerene Thin Films by Controlled Solvent Annealing. *Adv. Funct. Mater.* **2013**, *23*, 1701−1710.
(14) Yin, W.; Dadmun, M. A New Model for the Morphology of P3HT/PCBM Organic Photovoltaics from Small-Angle Neutron Scattering: Rivers and Streams. *ACS Nano* **2011**, *5*, 4756−4768.
(15) Ding, K.; Liu, X.; Forrest, S. R. Charge Transfer and Collection in Dilute Organic Donor−Acceptor Heterojunction Blends. *Nano Lett.* **2018**, *18*, 3180−3184.
(16) Dou, L.; You, J.; Yang, J.; Chen, C.-C.; He, Y.; Murase, S.; Moriarty, T.; Emery, K.; Li, G.; Yang, Y. Tandem Polymer Solar Cells Featuring a Spectrally Matched Low-Bandgap Polymer. *Nat. Photonics* **2012**, *6*, 180−185.
(17) Collins, B. A.; Gann, E.; Guignard, L.; He, X.; McNeill, C. R.; Ade, H. Molecular Miscibility of Polymer-Fullerene Blends. *J. Phys. Chem. Lett.* **2010**, *1*, 3160−3166.
(18) Li, W.; Hendriks, K. H.; Furlan, A.; Roelofs, W. S. C.; Wienk, M. M.; Janssen, R. A. J. Universal Correlation between Fibril Width and Quantum Efficiency in Diketopyrrolopyrrole-Based Polymer Solar Cells. *J. Am. Chem. Soc.* **2013**, *135*, 18942−18948.
(19) Stapleton, A.; Vaughan, B.; Xue, B.; Sesa, E.; Burke, K.; Zhou, X.; Bryant, G.; Werzer, O.; Nelson, A.; David Kilcoyne, a. L.; et al. A Multilayered Approach to Polyfluorene Water-Based Organic Photovoltaics. *Sol. Energy Mater. Sol. Cells* **2012**, *102*, 114−124.
(20) Xie, C.; Classen, A.; Späth, A.; Tang, X.; Min, J.; Meyer, M.; Zhang, C.; Li, N.; Osvet, A.; Fink, R. H.; et al. Overcoming Microstructural Limitations in Water Processed Organic Solar Cells by Engineering Customized Nanoparticulate Inks. *Adv. Energy Mater.* **2018**, *8*, 1702857.
(21) Ulum, S.; Holmes, N.; Darwis, D.; Burke, K.; David Kilcoyne, a. L.; Zhou, X.; Belcher, W.; Dastoor, P. Determining the Structural Motif of P3HT:PCBM Nanoparticulate Organic Photovoltaic Devices. *Sol. Energy Mater. Sol. Cells* **2013**, *110*, 43−48.
(22) Ulum, S.; Holmes, N.; Barr, M.; Kilcoyne, A. L. D.; Gong, B. B.; Zhou, X.; Belcher, W.; Dastoor, P. The Role of Miscibility in Polymer:fullerene Nanoparticulate Organic Photovoltaic Devices. *Nano Energy* **2013**, *2*, 897−905.
(23) Holmes, N. P.; Burke, K. B.; Sista, P.; Barr, M.; Magurudeniya, H. D.; Stefan, M. C.; Kilcoyne, A. L. D.; Zhou, X.; Dastoor, P. C.; Belcher, W. J. Nano-Domain Behaviour in P3HT:PCBM Nanoparticles, Relating Material Properties to Morphological Changes. *Sol. Energy Mater. Sol. Cells* **2013**, *117*, 437−445.
(24) Holmes, N. P.; Nicolaidis, N.; Feron, K.; Barr, M.; Burke, K. B.; Al-Mudhaffer, M.; Sista, P.; Kilcoyne, a. L. D.; Stefan, M. C.; Zhou, X.; et al. Probing the Origin of Photocurrent in Nanoparticulate Organic Photovoltaics. *Sol. Energy Mater. Sol. Cells* **2015**, *140*, 412−421.
(25) Holmes, N. P.; Vaughan, B.; Williams, E. L.; Kroon, R.; Anderrson, M. R.; Kilcoyne, A. L. D.; Sonar, P.; Zhou, X.; Dastoor, P. C.; Belcher, W. J. Diketopyrrolopyrrole-Based Polymer:fullerene Nanoparticle Films with Thermally Stable Morphology for Organic Photovoltaic Applications. *MRS Commun.* **2017**, *7*, 67−73.
(26) Scarongella, M.; De Jonghe-Risse, J.; Buchaca-Domingo, E.; Causa', M.; Fei, Z.; Heeney, M.; Moser, J.-E.; Stingelin, N.; Banerji, N. A Close Look at Charge Generation in Polymer:fullerene Blends with Microstructure Control. *J. Am. Chem. Soc.* **2015**, *137*, 2908−2918.
(27) Mateker, W. R.; McGehee, M. D. Progress in Understanding Degradation Mechanisms and Improving Stability in Organic Photovoltaics. *Adv. Mater.* **2017**, *29*, 1603940.
(28) Gehan, T. S.; Bag, M.; Renna, L. A.; Shen, X.; Algaier, D. D.; Lahti, P. M.; Russell, T. P.; Venkataraman, D. Multiscale Active Layer Morphologies for Organic Photovoltaics Through Self-Assembly of Nanospheres. *Nano Lett.* **2014**, *14*, 5238−5243.
(29) Chen, T. A.; Wu, X.; Rieke, R. D. Regiocontrolled Synthesis of Poly(3-Alkylthiophenes) Mediated by Rieke Zinc: Their Characterization and Solid-State Properties. *J. Am. Chem. Soc.* **1995**, *117*, 233−244.
(30) Clark, J.; Silva, C.; Friend, R. H.; Spano, F. C. Role of Intermolecular Coupling in the Photophysics of Disordered Organic Semiconductors: Aggregate Emission in Regioregular Polythiophene. *Phys. Rev. Lett.* **2007**, *98*, 206406.
(31) Spano, F. C. The Spectral Signatures of Frenkel Polarons in H- and J-Aggregates. *Acc. Chem. Res.* **2010**, *43*, 429−439.
(32) Spano, F. C.; Clark, J.; Silva, C.; Friend, R. H. Determining Exciton Coherence from the Photoluminescence Spectral Line Shape in poly(3-Hexylthiophene) Thin Films. *J. Chem. Phys.* **2009**, *130*, 74904.
(33) Niles, E. T.; Roehling, J. D.; Yamagata, H.; Wise, A. J.; Spano, F. C.; Moule, A. J.; Grey, J. K. J-Aggregate Behavior in Poly-3-Hexylthiophene Nanofibers. *J. Phys. Chem. Lett.* **2012**, *3*, 259−263.
(34) Barnes, M. D.; Baghar, M. Optical Probes of Chain Packing Structure and Exciton Dynamics in Polythiophene Films, Composites, and Nanostructures. *J. Polym. Sci., Part B: Polym. Phys.* **2012**, *50*, 1121−1129.
(35) Pedersen, E. B. L.; Pedersen, M. C.; Simonsen, S. B.; Brandt, R. G.; Böttiger, A. P. L.; Andersen, T. R.; Jiang, W.; Xie, Z. Y.; Krebs, F. C.; Arleth, L.; et al. Structure and Crystallinity of Water Dispersible Photoactive Nanoparticles for Organic Solar Cells. *J. Mater. Chem. A* **2015**, *3*, 17022−17031.

DOI: 10.1021/acs.chemmater.8b03222
Chem. Mater. XXXX, XXX, XXX−XXX

(36) Cook, S.; Ohkita, H.; Kim, Y.; Benson-Smith, J. J.; Bradley, D. D. C.; Durrant, J. R. A Photophysical Study of PCBM Thin Films. *Chem. Phys. Lett.* **2007**, *445*, 276−280.
(37) Nicolaidis, N. C.; Routley, B. S.; Holdsworth, J. L.; Belcher, W. J.; Zhou, X.; Dastoor, P. C. Fullerene Contribution to Photocurrent Generation in Organic Photovoltaic Cells. *J. Phys. Chem. C* **2011**, *115*, 7801−7805.
(38) Al-Mudhaffer, M. F.; Griffith, M. J.; Feron, K.; Nicolaidis, N. C.; Cooling, N. A.; Zhou, X.; Holdsworth, J.; Belcher, W. J.; Dastoor, P. C. The Origin of Performance Limitations in Miniemulsion Nanoparticulate Organic Photovoltaic Devices. *Sol. Energy Mater. Sol. Cells* **2018**, *175*, 77−88.
(39) Watkins, P. K.; Walker, A. B.; Verschoor, G. L. B. Dynamical Monte Carlo Modelling of Organic Solar Cells: The Dependence of Internal Quantum Efficiency on Morphology. *Nano Lett.* **2005**, *5*, 1814−1818.
(40) Feron, K.; Zhou, X.; Belcher, W. J.; Dastoor, P. C. Exciton Transport in Organic Semiconductors: Förster Resonance Energy Transfer Compared with a Simple Random Walk. *J. Appl. Phys.* **2012**, *111*, 44510.
(41) Athanasopoulos, S.; Emelianova, E. V.; Walker, A. B.; Beljonne, D. Exciton Diffusion in Energetically Disordered Organic Materials. *Phys. Rev. B: Condens. Matter Mater. Phys.* **2009**, *80*, 195209.
(42) Feron, K.; Cave, J. M.; Thameel, M. N.; O'Sullivan, C. O.; Kroon, R.; Andersson, M. R.; Zhou, X.; Fell, C. J.; Belcher, W. J.; Walker, A. B.; et al. Utilizing Energy Transfer in Binary and Ternary Bulk Heterojunction Organic Solar Cells. *ACS Appl. Mater. Interfaces* **2016**, *8*, 20928−20937.
(43) Cook, S.; Katoh, R.; Furube, A. Exciton Splitting in Nanoscale Phase-Separated Polythiophene:fullerene Solar Cell Blends. *J. Nanoelectron. Optoelectron.* **2010**, *5*, 115−119.
(44) Shaw, P. E.; Ruseckas, A.; Samuel, I. D. W. Exciton Diffusion Measurements in poly(3-Hexylthiophene). *Adv. Mater.* **2008**, *20*, 3516−3520.
(45) Mikhnenko, O. V.; Lin, J.; Shu, Y.; Anthony, J. E.; Blom, P. W. M.; Nguyen, T.-Q.; Loi, M. A. Effect of Thermal Annealing on Exciton Diffusion in a Diketopyrrolopyrrole Derivative. *Phys. Chem. Chem. Phys.* **2012**, *14*, 14196−14201.
(46) Heitzer, H. M.; Savoie, B. M.; Marks, T. J.; Ratner, M. A. Organic Photovoltaics: Elucidating the Ultra-Fast Exciton Dissociation Mechanism in Disordered Materials. *Angew. Chem., Int. Ed.* **2014**, *53*, 7456−7460.
(47) Menke, S. M.; Holmes, R. J. Exciton Diffusion in Organic Photovoltaic Cells. *Energy Environ. Sci.* **2014**, *7*, 499−512.
(48) Peumans, P.; Yakimov, A.; Forrest, S. R. Small Molecular Weight Organic Thin-Film Photodetectors and Solar Cells. *J. Appl. Phys.* **2003**, *93*, 3693−3723.
(49) Leman, D.; Kelly, M. A.; Ness, S.; Engmann, S.; Herzing, A.; Snyder, C.; Ro, H. W.; Kline, R. J.; DeLongchamp, D. M.; Richter, L. J. In Situ Characterization of Polymer−Fullerene Bilayer Stability. *Macromolecules* **2015**, *48*, 383−392.
(50) Müller, C. On the Glass Transition of Polymer Semiconductors and Its Impact on Polymer Solar Cell Stability. *Chem. Mater.* **2015**, *27*, 2740−2754.
(51) Sharma, A.; Pan, X.; Campbell, J. A.; Andersson, M. R.; Lewis, D. A. Unravelling the Thermomechanical Properties of Bulk Heterojunction Blends in Polymer Solar Cells. *Macromolecules* **2017**, *50*, 3347−3354.
(52) Martín, J.; Stingelin, N.; Cangialosi, D. Direct Calorimetric Observation of the Rigid Amorphous Fraction in a Semiconducting Polymer. *J. Phys. Chem. Lett.* **2018**, *9*, 990−995.
(53) Chen, D.; Nakahara, A.; Wei, D.; Nordlund, D.; Russell, T. P. P3HT/PCBM Bulk Heterojunction Organic Photovoltaics: Correlating Efficiency and Morphology. *Nano Lett.* **2011**, *11*, 561−567.
(54) Chen, D.; Liu, F.; Wang, C.; Nakahara, A.; Russell, T. P. Bulk Heterojunction Photovoltaic Active Layers via Bilayer Interdiffusion. *Nano Lett.* **2011**, *11*, 2071−2078.
(55) Treat, N. D.; Mates, T. E.; Hawker, C. J.; Kramer, E. J.; Chabinyc, M. L. Temperature Dependence of the Diffusion Coefficient of PCBM in Poly(3-Hexylthiophene). *Macromolecules* **2013**, *46*, 1002−1007.
(56) Lee, K. H.; Schwenn, P. E.; Smith, A. R. G.; Cavaye, H.; Shaw, P. E.; James, M.; Krueger, K. B.; Gentle, I. R.; Meredith, P.; Burn, P. L. Morphology of All-Solution-Processed "bilayer" organic Solar Cells. *Adv. Mater.* **2011**, *23*, 766−770.
(57) He, X.; Collins, B. a; Watts, B.; Ade, H.; McNeill, C. R. Studying Polymer/fullerene Intermixing and Miscibility in Laterally Patterned Films with X-Ray Spectromicroscopy. *Small* **2012**, *8*, 1920−1927.
(58) Wang, D.; Nakajima, K.; Liu, F.; Shi, S.; Russell, T. P. Nanomechanical Imaging of the Diffusion of Fullerene into Conjugated Polymer. *ACS Nano* **2017**, *11*, 8660−8667.
(59) Iovu, M. C.; Sheina, E. E.; Gil, R. R.; McCullough, R. D. Experimental Evidence for the Quasi-"Living" Nature of the Grignard Metathesis Method for the Synthesis of Regioregular Poly(3-Alkylthiophenes). *Macromolecules* **2005**, *38*, 8649−8656.
(60) Lee, S. S.; Loo, Y.-L. Structural Complexities in the Active Layers of Organic Electronics. *Annu. Rev. Chem. Biomol. Eng.* **2010**, *1*, 59−78.
(61) Brumboiu, I. E.; Anselmo, a. S.; Brena, B.; Dzwilewski, a.; Svensson, K.; Moons, E. Near-Edge X-Ray Absorption Fine Structure Study of the C60-Derivative PCBM. *Chem. Phys. Lett.* **2013**, *568*−*569*, 130−134.
(62) Kilcoyne, A. L. D.; Tyliszczak, T.; Steele, W. F.; Fakra, S.; Hitchcock, P.; Franck, K.; Anderson, E.; Harteneck, B.; Rightor, E. G.; Mitchell, G. E.; et al. Interferometer-Controlled Scanning Transmission X-Ray Microscopes at the Advanced Light Source. *J. Synchrotron Radiat.* **2003**, *10*, 125−136.
(63) McNeill, C. R.; Watts, B.; Thomsen, L.; Belcher, W. J.; Greenham, N. C.; Dastoor, P. C. Nanoscale Quantitative Chemical Mapping of Conjugated Polymer Blends. *Nano Lett.* **2006**, *6*, 1202−1206.
(64) Lloyd, M. T.; Lim, Y.; Malliaras, G. G.; Lloyd, M. T.; Lim, Y.; Malliaras, G. G. Two-Step Exciton Dissociation in poly(3-Hexylthiophene)/fullerene Heterojunctions. *Appl. Phys. Lett.* **2008**, *92*, 143308.

DOI: 10.1021/acs.chemmater.8b03222
Chem. Mater. XXXX, XXX, XXX−XXX